

P-wave velocity structure beneath the northern Antarctic Peninsula: evidence of a steeply subducting slab and a deep-rooted low-velocity anomaly beneath the central Bransfield Basin

Yongcheol Park,¹ Kwang-Hee Kim,² Joochan Lee,¹ Hyun Jae Yoo¹ and Milton P. Plasencia L.³

¹The Korea Polar Research Institute, Incheon, South Korea. E-mail: ypark@kopri.re.kr

²The Korea Ocean Research and Development Institute, Ansan, South Korea

³Istituto Nazionale di Oceanografia e di Geofisica Sperimentale – OGS, Italia

Accepted 2012 September 17. Received 2012 September 10; in original form 2012 May 12

SUMMARY

Upper-mantle structure between 100 and 300 km depth below the northern Antarctic Peninsula is imaged by modelling *P*-wave traveltimes residuals from teleseismic events recorded on the King Sejong Station (KSJ), the Argentinean/Italian stations (JUBA and ESPZ), an IRIS/GSN Station (PMSA) and the Seismic Experiment in Patagonia and Antarctica (SEPA) broad-band stations. For measuring traveltimes residuals, we applied a multichannel cross-correlation method and inverted for upper-mantle structure using VanDecar's method. The new 3-D velocity model reveals a subducted slab with a $\sim 70^\circ$ dip angle at 100–300 km depth and a strong low-velocity anomaly confined below the SE flank of the central Bransfield Basin. The low velocity is attributed to a thermal anomaly in the mantle that could be as large as 350–560 K and which is associated with high heat flow and volcanism in the central Bransfield Basin. The low-velocity zone imaged below the SE flank of the central Bransfield Basin does not extend under the northern Bransfield Basin, suggesting that the rifting process in that area likely involves different geodynamic processes.

Key words: Body waves; Broad-band seismometers; Seismic tomography; Subduction zone processes; Continental margins: convergent; Antarctica.

STUDY AREA

The South Shetland Islands–Antarctic Peninsula region is a very complex active place in geodynamics because of ongoing, slow subduction and its related phenomena, such as extensional basin in the Bransfield Strait (Fig. 1), a series of fractures and neovolcanic activities. The Antarctic Peninsula was a part of the Gondwana supercontinent and experienced subduction from the Mesozoic to the late Cenozoic. Magnetic anomaly patterns and seafloor bathymetry reflect recent Cenozoic active margin dynamics. Barker (1982) and Larter & Barker (1991a) reported a sequence of successive ridge–trench collisions, which started in the south of the peninsula ca. 50 Ma (Larter *et al.* 2002; Eagles *et al.* 2004, 2009; Scheuer *et al.* 2006). The ridge–trench collisions migrated progressively northwards reaching the Biscoe Fracture Zone (BFZ) ~ 16 Ma, and the South and North Anvers fracture zones (SAFZ and NAFZ) ~ 10 and ~ 6 Ma, respectively. After each of the ridge–trench collisions, both subduction and spreading stopped along the corresponding section of the margin, and the trench topography disappeared (Tucholke & Houtz 1976; Larter & Barker 1991b). The progression of ridge–trench collision and associated cessation of subduction continued up to the Hero Fracture Zone (HFZ) ~ 4 – ~ 2.5 Ma. Today, the subduction is taking place only between

the Hero and the Shackleton fracture zones. The remnant plate between the Antarctic–Phoenix spreading ridge (APSR) and the south Shetland Trench (SST) has been referred to as the ‘Phoenix’, ‘Aluk’, or ‘Drake’ Plate (Barker 1982; Larter & Barker 1991a; Larter *et al.* 2002). The age of the subducted Phoenix Plate at the trench increases from 14 Ma near the ridge segment south of the Hero Fracture Zone to 23 Ma near the Shackleton Fracture Zone (Barker 1982). After the collision of the Hero Fracture Zone with the Antarctic Peninsula, spreading stopped on the last segments of the Antarctic–Phoenix spreading centre.

The Bransfield Strait Basin, located between the South Shetland Islands and the northern end of the Antarctic Peninsula, is ~ 100 km wide and ~ 400 km long (Barker 1982; Gambôa & Maldonado 1990; Lawver *et al.* 1995) and is divided into the south, central and north Bransfield basins on the basis of bathymetry (Fig. 2) and gravity anomalies (Sandwell 1992; Lawver *et al.* 1995). The south Bransfield Basin is outlined by the ~ 1000 m depth contour, which trends southwest from Deception Island (DI, Canals *et al.* 2000). The central Bransfield Basin is bounded by DI and Bridgeman Island (BI) and locally exceeds ~ 2000 m depth contour (Lawver *et al.* 1996; Gràcia *et al.* 1997). The north Bransfield Basin is deepest (~ 2700 m) and exhibits the deepest negative gravity anomaly of approximately -30 mGal between BI and Clarence Island (CI,

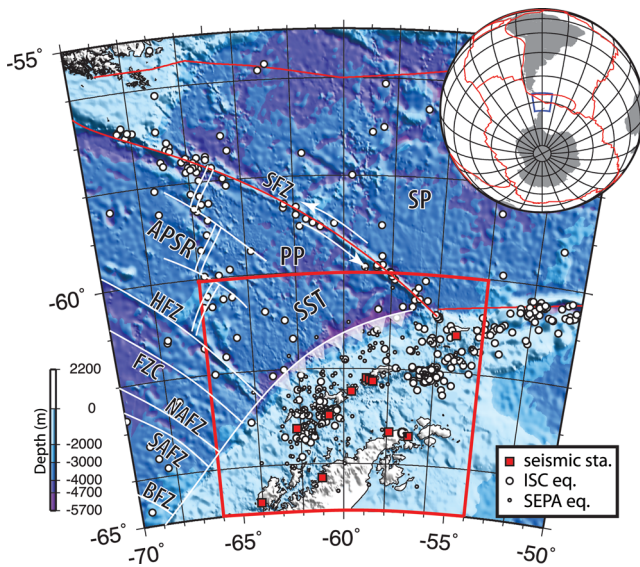


Figure 1. Map of the study area showing topography, seismic stations, earthquake locations and major tectonic features. Red rectangle indicates the area of the map views plotted in Figs 2–5. Large and small circles are earthquake locations reported by International Seismological Centre (ISC) between 1960 and present, and regional events by Robertson Maurice *et al.* (2003) from SEPA data, respectively. APSR, Antarctic Phoenix Spreading Ridge; BFZ, Biscoe Fracture Zone; HFZ, Hero Fracture Zone; NAFZ, North Anvers Fracture Zone; SAFZ, South Anvers Fracture Zone; PP, Phoenix Plate; SFZ, Shackleton Fracture Zone; SST, South Shetland Trench and SP, Scotia Plate.

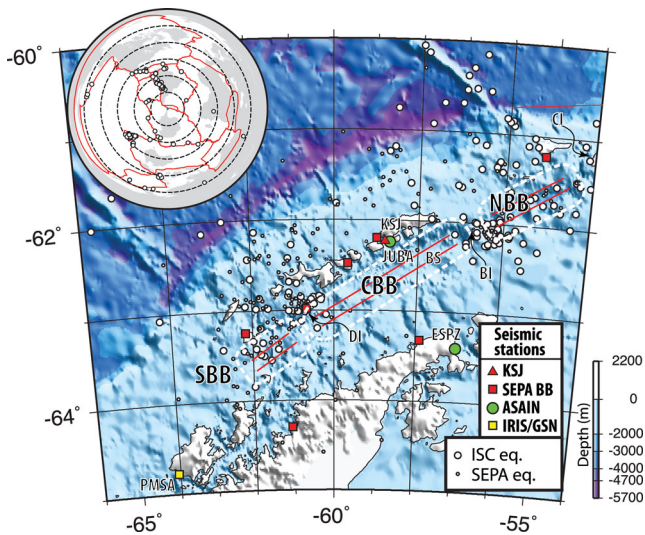


Figure 2. Locations of seismic stations and teleseismic earthquakes (inset map) used in the study. White dashed rectangles indicate south (SBB), central (CBB) and north Bransfield Basin (NBB) from south to north, respectively. DI, Deception Island; BI, Bridgeman Island and CI, Clarence Island.

Lawver *et al.* 1995, 1996). The strait has been considered an extensional marginal basin that developed behind the SST and the extinct South Shetland Island arc. In spite of a lack of active South Shetland Islands arc volcanism, the strait is regarded as a backarc rift using high-quality multichannel seismic data by Gambôa & Maldonado (1990). The timing of rifting in the basin remains unclear. The magnetic anomalies formed at the Antarctic–Phoenix Ridge suggest that the rift in the strait started ~ 4 Ma at the same

time as spreading stopped at the spreading centre (Barker 1982; Larter & Barker 1991a; Livermore *et al.* 2000). Larter & Barker (1991a) showed that there was an abrupt decrease in spreading rate at the young end of anomaly C3B (~ 6.9 Ma), and it could be suggested that this change is just as likely to be related to the onset of rifting in Bransfield Strait as the final stoppage of spreading. However, radiometric dates from the dyke intrusion transversal to the direction of the Bransfield Rift in the King George Island showed that the rifting may have begun between 26 and 22 Ma (Smellie *et al.* 1984; Birkenmajer 1992). Gonzalez-Ferran (1991) analysed aeromagnetic data from the Bransfield Basin and concluded that rifting had produced 5–15 km of extension over the past 2 Ma with a total spreading rate of 2.5–7.5 mm yr⁻¹. Gràcia *et al.* (1996) interpreted a maximum age of seafloor spreading of 0.7 Ma and a rate of 0.83 mm yr⁻¹ for total spreading rate. Current extension in the Bransfield Strait is in an NW–SE direction at a rate of ~ 7 mm yr⁻¹ measured by geodetic GPS analysis (Dietrich *et al.* 2004). Seismicity studies reported intermediate-focus earthquakes and suggested that the SST is an active subduction (Ibáñez *et al.* 1997; Robertson Maurice *et al.* 2003).

The crustal and shallow upper-mantle structures in the Bransfield Basin have been extensively studied using refractive and reflective seismic surveys (e.g. Ashcroft 1972; Guterch *et al.* 1985; Gambôa & Maldonado 1990; Guterch *et al.* 1991; Grad *et al.* 1993; Barker & Austin 1994; Grad *et al.* 1997; Janik 1997; Barker & Austin 1998; Lee *et al.* 2000; Jin *et al.* 2002; Barker *et al.* 2003; Christeson *et al.* 2003; Janik *et al.* 2006), magnetic and gravity analyses (e.g. Johnson 1999; Yegorova *et al.* 2011) and regional surface wave dispersions and receiver function studies (e.g. Vuan *et al.* 1999, 2000, 2001, 2005a,b). The deeper structure of the area, however, has not yet been studied. This study presents the first model of a subducting slab up to 300 km deep based on teleseismic earthquake data and reveals a low-velocity anomaly beneath the central Bransfield Strait.

DATA AND MODELLING

Teleseismic earthquake data used in this study were obtained from two sets of seismic stations. The Seismic Experiment in Patagonia and Antarctica (SEPA) (Robertson Maurice *et al.* 2003) provided broad-band data, and the King Sejong Station (KSJ) together with the Jubany (JUBA) and Esperanza (ESPZ) broad-band seismic stations of the ASAIN network (managed by a cooperation project between the Argentinean Direccion Nacional del Antartico and the Italian Programma Nazionale di Ricerca in Antartide) and the IRIS/GSN Station (PMSA) collectively provided seismic data (Fig. 2). The SEPA project included seven broad-band land stations and 14 ocean bottom seismometers (OBSs); due to data availability, this study used only the data from land stations observed between 1997 and 1999 (red squares in Fig. 2). The Korea Polar Research Institute (KOPRI) has operated a permanent seismic station (KSJ) with a Q4124 digital acquisition system and a Streckeisen STS-2 broad-band seismometer since December 2001 (red triangle in Fig. 2). Data recorded on KSJ and PMSA stations from 2007 to 2009 were used to calculate relative traveltimes with the 2007–2009 data from JUBA and ESPZ (green circles in Fig. 2).

The combined data set includes 347 ray paths for *P*- and *PKP*-wave arrivals from 95 earthquakes that have correlation coefficients above 0.8. All of the stations on islands have low signal-to-noise ratios, and only 95 earthquakes yielded reliable measurements. The inset map in Fig. 2 shows equal-area projection of major plate boundaries and locations of teleseismic events centred on the KSJ seismic station (62.2253°S and 58.7959°W). The events were

distributed over a wide range of backazimuths with the large concentration coming from the Peru–Chile Trench and the Tonga–Kermadec Trench. The broad-band data were filtered with a zero-phase two-pole Butterworth filter between 0.5 and 5.0 Hz, and relative *P*-wave traveltimes were then calculated using a multichannel cross-correlation (MCCC) method (VanDecar & Crosson 1990).

The traveltimes were inverted for a 3-D velocity model using the method of VanDecar (1991). The IASP91 model (Kennett & Engdahl 1991) was used to initiate the inversion. For the inversion, a model was parameterized using a grid of 20,608 nodes, with 28 depth nodes from the surface to 1,000 km, 23 latitudinal nodes between 59°S and 67°S and 32 longitudinal nodes between 53.5°W and 65.5°W. The horizon node spaces for the latitude and longitude were a quarter and one-third degrees, respectively. The vertical node space was 25 km in the inner region of the model (61.5°S–65.5°S, 55.5°W–63.5°W and 0–200 km depth), 30 km between 200 and 800 km depth and 100 km between 800 and 1,000 km depth. Horizontally, the node space increased to a half degree in the outer regions of the model. During the inversion procedure, station static terms were computed to compensate for traveltimes arising from the heterogeneity in the crustal and uppermost mantle structure directly beneath each station. Optimal smoothing and flattening parameters were selected through investigation of trade-off curves of relative traveltimes rms misfit versus model roughness. Optimal parameters resulted in a *P*-wave velocity model with a traveltimes residual reduction of 86.6 per cent, yielding a final rms residual of 0.067 s after 2000 inversion iterations.

INVERTED MODEL

Fig. 3 shows horizontal depth slices (a)–(d) and vertical cross-sections (e)–(f) of the *P*-wave velocity model. The structure below 300 km depth and above 50 km depth is not shown because of the limited number of crossing ray paths below and above the 50 and 300 km depth interval. The depth slices (Figs 3a–d) show fast velocity anomalies of $\delta V_p = 0.5$ –1.8 per cent, confined mainly to the SE of the SST, and the largest amplitude anomaly is located beneath the South Shetland Islands. The fast anomalies trend SW–NE parallel to the SST, and move to the SE with increasing depth. The fast-velocity zone does not appear beneath the Antarctic Peninsula. The model shows a low-velocity anomaly of up to $\delta V_p = \sim -1.2$ per cent beneath the SE flank of the central Bransfield Basin and the northern part of the Antarctic Peninsula at deeper depths (Figs 3c and d). Another low-velocity anomaly is at the northern edge of the model.

Profile A–A' crosses the central basin axis from the SST to the Antarctic Peninsula, and shows the velocity contrast between the higher velocity zone dipping steeply to the SE from the SST and the lower velocity under the SE flank of the Bransfield Strait and the Antarctic Peninsula (Fig. 3e). Across this profile is an approximately 3 per cent lateral variation in the *P*-wave velocity between depths of 100 and 200 km. The Bransfield Strait has a very asymmetrical cross-section and the profile B–B' runs to the SE of the deepest part of the basin (Fig. 2). The vertical slice B–B' in Fig. 3(f) shows a small low-velocity anomaly beneath the central parts of the Bransfield Strait.

RESOLUTION TESTS

Our model was inverted from only 347 *P*-wave arrivals for the study area bigger than ~ 1000 km². This limited number of ray paths could

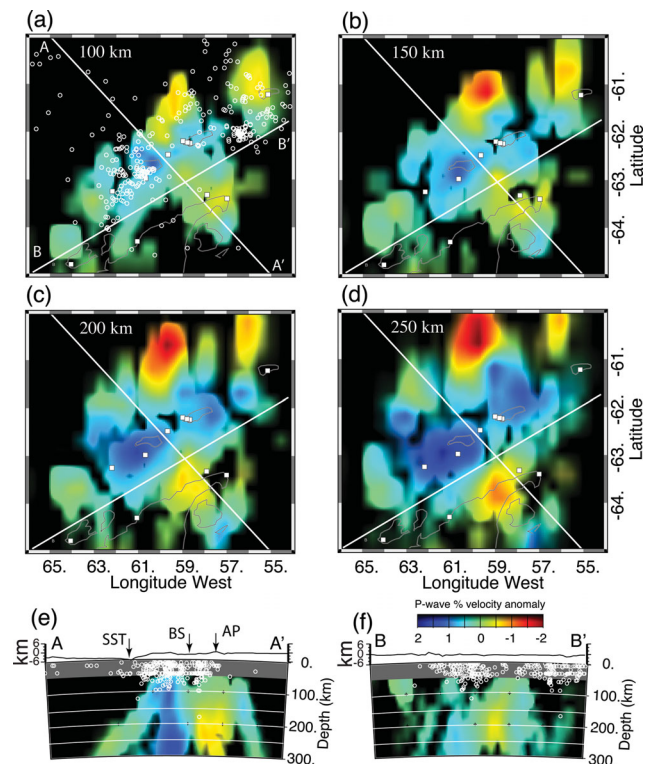


Figure 3. *P*-wave velocity model. (a)–(d) Horizontal cross-sections through the model are shown for depths of 100, 150, 200 and 250 km. (e) and (f) Vertical cross-sections each white line in (a). Areas with hit counts of less than 2 are darkened. In (e)–(f), SST, South Shetland Trench; BS, Bransfield Strait and AP, Antarctic Peninsula.

not resolve small structure such as a checkerboard pattern consisting of spheres with a radius of less than 50 km (Fig. S1, Supporting Information). Therefore, to examine how the model might be able to resolve detail structure, target resolution tests were undertaken. In the target resolution test, an assumed structure inferred from the geodynamic setting of the study area is employed to calculate synthetic traveltimes along the ray paths, and then a model is inverted from them. The results allow evaluation of how the target structure could be resolved using the data set. Target structures that were set to be resolved from our model were a slab-like fast-velocity anomaly and a plume-like low-velocity anomaly. The fast-slab anomaly was generated with 120-km-wide Gaussian spheres starting along the SST at the surface and extending to 500 km depth with different angles. The low-velocity anomaly was produced with 80-km-wide Gaussian spheres from 50 to 120 km depth beneath the Bransfield Basin. Figs 4–7 show the results of resolution tests with different slab dip angles and shapes of low-velocity anomalies. Fig. 4 shows the model that most closely resembles the model derived from the inversion of real data. The recovered velocity structure indicates that a steeply dipping fast-velocity structure can be resolved (Fig. 4f). The resolution tests show that low-velocity zones extending down to 120 km depth are smeared down to 250 km depth and shifted to the southeast with increasing depths. The results from other resolution tests will be discussed in the next section.

DISCUSSION

The main features of the model are a linear trended fast-velocity anomaly parallel to the SST and a low-velocity anomaly beneath the SE flank of the central Bransfield Basin. The fast-velocity anomaly

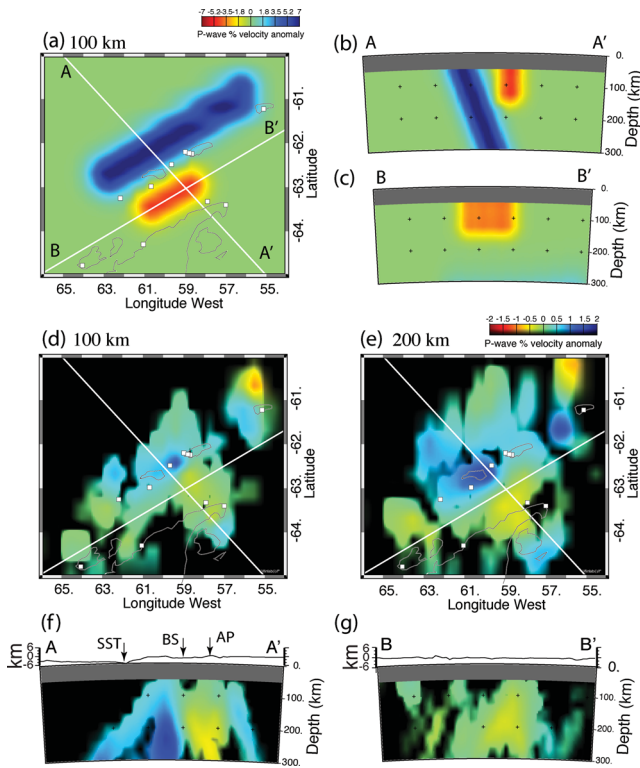


Figure 4. Synthetic resolution test of a subducting slab at $\delta = 70^\circ$ for the *P*-wave model using 80-km-diameter Gaussian spheres with +7 and -5 per cent peak velocity anomaly. (a) Input model with station locations in map view, and (b) and (c) input model cross-sections along A–A' and B–B'. (d)–(g) Recovered model from the inversion with area where hit counts <2 in black: horizontal cross-sections at depths of (d) 100 km and (e) 200 km and vertical cross-sections along (f) A–A' and (g) B–B'.

may indicate a subducting slab, which is consistent with underthrusting of the former Phoenix Plate beneath the South Shetland block. Such an interpretation has been reported by many previous studies of reflection and refraction experiments (Grad *et al.* 1993, 1997; Maldonado *et al.* 1994; Kim *et al.* 1995; Barker & Austin 1998), gravity and magnetic anomaly analyses (Yegorova *et al.* 2011) and studies of seismicity distributions (Forsyth 1975; Pelayo & Wiens 1989; Robertson Maurice *et al.* 2003). Grad *et al.* (1993) modelled 2-D structure using data from active seismic exploration. Their model showed the lithospheric boundary of the subducting slab with a shallow dip angle ($\delta \sim 25^\circ$) at depths from 35 to 80 km. The present models, however, show that the dip angle of the subducting Phoenix Plate is very steep ($\delta \sim 70^\circ$) at depths below 100 km. To verify whether the steeply dipping fast-velocity anomaly is a real structure, several slab-like resolution tests were performed with different dip angles. According to the resolution test with a shallower dip angle ($< 65^\circ$), the inversion could not reproduce the model inverted from observed data (Fig. 5), and the best dip angle was determined to be $\delta = 70^\circ$ (Fig. 4). The resolution test only loosely supports the presence of a structure, but is the best model inverted from the teleseismic data observed so far. The determined dip angle is similar to that of the South Sandwich Trench ($\sim 67^\circ$) where backarc spreading is well developed (Jarrard 1986; Stern 2002; Larter *et al.* 2003; Livermore 2003; Heuret & Lallemand 2005), and may be a response to slab rollback mechanism related to extensional activity in the Bransfield Basin as well as seaward migration of the trench (e.g. Barker 1982; Smellie *et al.* 1984; Lawver *et al.* 1995; Barker & Austin 1998).

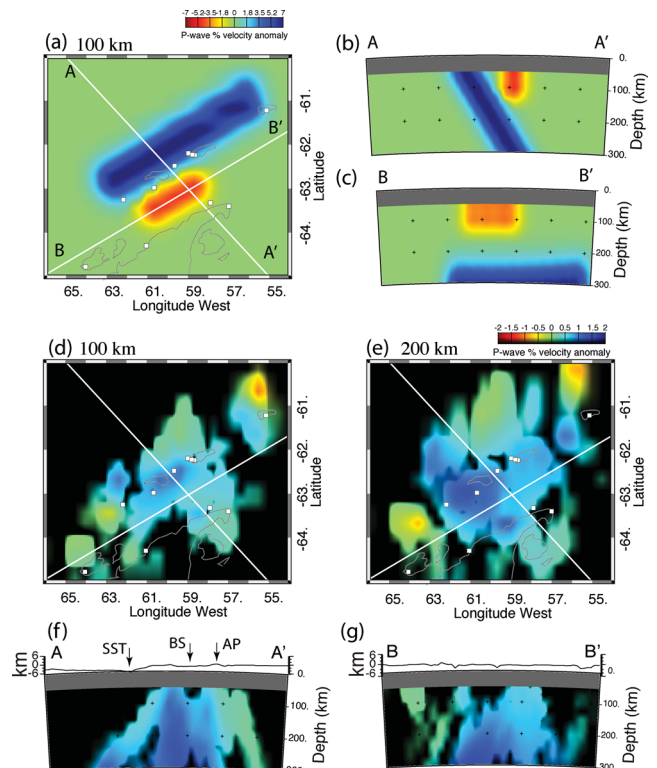


Figure 5. Synthetic resolution test of a subducting slab at $\delta = 60^\circ$ for the *P*-wave model using 80-km-diameter Gaussian spheres with +7 and -5 per cent peak velocity anomaly. (a) Input model with station locations in map view, and (b) and (c) input model cross-sections along A–A' and B–B'. (d)–(g) Recovered model from the inversion with area where hit counts <2 in black: horizontal cross-sections at depths of (d) 100 km and (e) 200 km and vertical cross-sections along (f) A–A' and (g) B–B'.

The other characteristics of the model are low-velocity anomalies at the northern edge of the model and beneath the SE flank of the central part of the Bransfield Basin. The low-velocity anomaly in the north could be an edge effect of the inversion procedure rather than a real structure. The low-velocity anomaly beneath the SE flank of the central Bransfield Basin does not extend to the northern basin. A number of resolution tests were performed using different shapes for the low-velocity anomaly. First, a linear low-velocity anomaly across the central to northern Bransfield Basin (Fig. 6) produced a low-velocity anomaly with maxima at $\sim 63^\circ$ S and $\sim 58^\circ$ W, which is farther north than the low-velocity anomaly in Fig. 3. This indicates that the low-velocity anomaly in the central Bransfield Basin could be real and suggests that there are no low-velocity anomalies deeper than 100 km depth in the northern Bransfield Basin. The final test examined whether the low-velocity anomaly spans the entire central Bransfield Basin or is confined to northern parts of the central Bransfield Basin, as suggested by the model. Two models were tested: one with a linear anomaly in the central Bransfield Basin (Fig. 4), and one with a spherical column-shape anomaly at the eastern edge of the central Bransfield Basin (Fig. 7). Both input models produce inverted models similar to the real model, but they are different in the amplitudes of the low-velocity anomaly. The 5 per cent low-velocity bodies in the input models are recovered at ~ 1.5 and ~ 0.5 per cent from the linear and column low-velocity models, respectively. The amplitudes of the recovered low-velocity anomalies are only ~ 30 and ~ 10 per cent of that of the input models due to smearing along ray paths using VanDecar's inversion method (e.g. Bastow *et al.* 2005; Benoit *et al.* 2006; Park *et al.* 2007). These

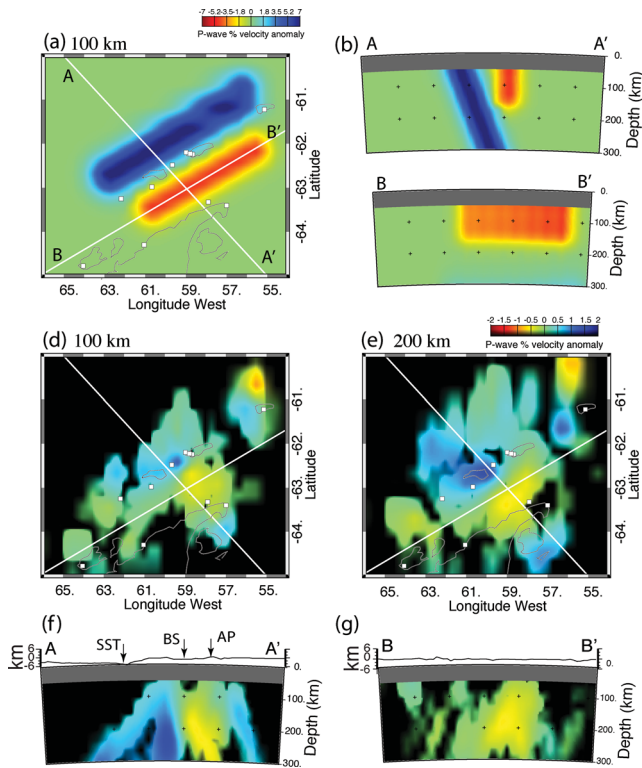


Figure 6. Synthetic resolution test of a subducting slab and a linear low-velocity anomaly for the P -wave model using 80-km-diameter Gaussian spheres with $+5$ and -5 per cent peak velocity anomaly. (a) Input model with station locations in map view, and (b) and (c) input model cross-sections along $A-A'$ and $B-B'$. (d)–(g) Recovered model from the inversion with area where hit counts < 2 in black: horizontal cross-sections at depths of (d) 100 km and (e) 200 km and vertical cross-sections along (f) $A-A'$ and (g) $B-B'$.

tests confirmed that the low-velocity anomaly in our real model could be inverted from a broad 5 per cent low-velocity anomaly beneath the entire central Bransfield Basin or from a smaller spherical column 80 km in diameter with an 8 per cent anomaly.

A lateral variation in seismic velocity model in the mantle can be explained with the temperature perturbation (Karato 1993). Using the method of Karato (1993) and $Q_P \sim 80$ for the continental rift area (Venkataraman *et al.* 2004), an 5 and 8 per cent reductions in P -wave velocity can be achieved with ~ 350 and ~ 560 K increases in temperature, respectively. The thermal variation beneath the Kenya and the Ethiopian Rift zones have been reported as ~ 280 K (Mechie *et al.* 1994) and ~ 240 K (Dugda *et al.* 2007), respectively. Inferred temperature variations from our model are relatively higher than variations in the Kenya and Ethiopian rifts. We assume that the input low-velocity anomaly up to 8 per cent in the resolution test might be exaggerated, and the broad low-velocity anomaly up to 5 per cent would provide appropriate results ($\Delta T = \sim 350$ K) to mineral rheology. The high-temperature anomaly would suggest that partial melts could be present in the upper mantle (Sato *et al.* 1988), which is consistent with both high seafloor heat-flow measurements (~ 626 mWm $^{-2}$) on surface (Lawver *et al.* 1995) and crustal thinning (Barker *et al.* 2003).

Refractive and reflective seismic studies undertaken over the past five decades imaged the crustal structure and thickness in the Bransfield Basin, but the details of crustal structure remain controversial (e.g. Ashcroft 1972; Guterch *et al.* 1991; Grad *et al.* 1993, 1997; Barker & Austin 1994, 1998; Janik 1997; Lee *et al.* 2000; Jin

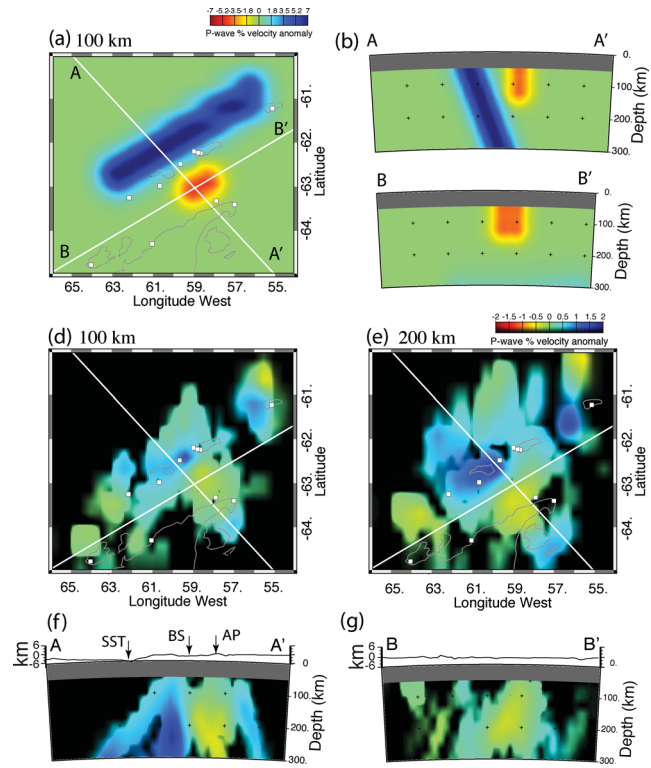


Figure 7. Synthetic resolution test of a subducting slab and a spherical column low-velocity anomaly for the P -wave model using 80-km-diameter Gaussian spheres with $+8$ and -5 per cent peak velocity anomaly. (a) Input model with station locations in map view, and (b) and (c) input model cross-sections along $A-A'$ and $B-B'$. (d)–(g) Recovered model from the inversion with area where hit counts < 2 in black: horizontal cross-sections at depths of (d) 100 km and (e) 200 km and vertical cross-sections along (f) $A-A'$ and (g) $B-B'$.

et al. 2002; Barker *et al.* 2003; Christeson *et al.* 2003; Vuan *et al.* 2005a; Janik *et al.* 2006). The Polish Antarctic geodynamic group suggested that the crustal thickness is ~ 30 km, and that an asymmetric high-velocity body is present at a depth interval from 13 to 38 km down to the Moho boundary (Guterch *et al.* 1985; Grad *et al.* 1993, 1997; Janik 1997; Janik *et al.* 2006). In contrast, Barker *et al.* (2003) presented thinner crustal thicknesses varying between ~ 10 and ~ 22 km in the central Bransfield Basin. Vuan *et al.* (2005b) presented a 1-D shear wave model for the central Bransfield Basin using regional Rayleigh and Love tomographies. Their model also showed low upper-mantle velocities extending down to depths exceeding 70 km, which is quite similar to the velocity profiles of the East African Kenya Rift (Keller *et al.* 1994), where pronounced low velocities have been observed as well (e.g. Green *et al.* 1991; Ritsema *et al.* 1998; Nyblade *et al.* 2000; Achauer & Masson 2002; Park & Nyblade 2006). The low-velocity anomaly in the central Bransfield Basin produced in this study supports the hypothesis that crustal thinning was associated with a hot upper mantle and soft lid velocity models (Vuan *et al.* 2000, 2005a,b).

To explain post ~ 3 Ma extension in the Bransfield Basin, two tectonic models have been proposed. The morphology and volcanic activity of the Bransfield Basin suggest that the Bransfield rift was initiated from the northeast either by a rollback process in the SST (e.g. Lawver *et al.* 1995; Gràcia *et al.* 1996; Barker & Austin 1998) or by a sinistral simple-shear couple between the Scotia and the Antarctic plates along the South Scotia Ridge Fault after spreading stopped on the Antarctic–Phoenix and western Scotia ridges and

then propagated towards the southeast. Volcanic activity in the north Bransfield Basin is diffuse but fissure-like eruptive features occur in the central Bransfield Basin (Lawver *et al.* 1996). Our model shows that the low-velocity anomaly at up to 120 km depth beneath the SE flank of central basin does not extend northwards. Thus, significant thermal anomalies are not present, or do not extend to in deeper than ~ 100 km depth in the northern basin. The presence of the low-velocity anomalies at up to 120 km depths beneath the SE flank of the central Bransfield Basin implies different tectonics between the rifting processes in the central and northern Bransfield basins. (Lawver *et al.* 1996)

CONCLUSIONS

P-wave tomographic images reveal a fast-velocity region parallel to the SST with a steep dip angle ($\sim 70^\circ$) below 100 km depth, and a strong low-velocity anomaly that is confined to the central Bransfield Basin. The fast anomaly indicates that a cold subducting slab of the Phoenix Plate is causing slab-pull owing to its negative buoyancy, thus generating an extensional backarc deformation. The low-velocity anomaly appears as a small area in the northern parts of the central Bransfield Basin, but the model used here cannot resolve whether the low-velocity anomaly occupies the entire central basin or only small parts as shown in the model. The low velocity can be attributed to a 350–560 K thermal anomaly in the upper mantle, depending on the intensity of velocity anomaly. This anomaly is reflected by high heat flow and volcanism in the central Bransfield Basin.

ACKNOWLEDGMENTS

We thank Christine Thomas, R. D. Larter and an anonymous reviewer for constructive comments. SEPA and PMSA data were obtained from the incorporated research Institutions for Seismology (IRIS) data management system (DMS). The GMT and SAC softwares have been used for this study. This work was supported by the Korea Polar Research Institute (grants PE12050 and PP12020).

REFERENCE

- Achauer, U. & Masson, F., 2002. Seismic tomography of continental rifts revisited: from relative to absolute heterogeneities, *Tectonophysics*, **358**, 17–37.
- Ashcroft, W.A., 1972. Crustal structure of the South Shetland Islands and Bransfield Strait, *British Antarctic Survey Sci. Rep.*, **66**, 43.
- Barker, P.F., 1982. The Cenozoic subduction history of the Pacific margin of the Antarctic Peninsula: ridge crest-trench interactions, *J. geol. Soc. London*, **139**, 787–801.
- Barker, D.H.N. & Austin, J.A., Jr., 1994. Crustal diapirism in Bransfield Strait, West Antarctica: evidence for distributed extension in marginal-basin formation, *Geology*, **22**, 657–660.
- Barker, D.H.N. & Austin, J.A., Jr., 1998. Rift propagation, detachment faulting, and associated magmatism in Bransfield Strait, Antarctic Peninsula, *J. geophys. Res.*, **103**, 24 017–24 043.
- Barker, D.H.N., Christeson, G.L., James, A., Austin, J. & Dalziel, I.W.D., 2003. Backarc basin evolution and cordilleran orogenesis: insights from new ocean-bottom seismograph refraction profiling in Bransfield Strait, Antarctica, *Geology*, **31**, 107–110.
- Bastow, I.D., Stuart, G.W., Kendall, J.M. & Ebinger, C.J., 2005. Upper-mantle seismic structure in a region of incipient continental breakup: northern Ethiopian rift, *Geophys. J. Int.*, **162**, 479–493.
- Benoit, M.H., Nyblade, A.A. & VanDecar, J.C., 2006. Upper mantle P wave speed variations beneath Ethiopia and the origin of the Afar Hotspot, *Geology*, **34**, 239–332.
- Birkenmajer, K., 1992. Evolution of the Bransfield basin and rift, West Antarctica, in *Recent Progress in Antarctic Earth Science*, pp. 405–410, eds Yoshida, Y. *et al.*, TERRAPUB, Tokyo.
- Canals, M., Urgeles, R. & Calafat, A.M., 2000. Deep sea-floor evidence of past ice streams off the Antarctic Peninsula, *Geology*, **28**, 31–34.
- Christeson, G.L., Barker, D.H.N., Austin, J.A., Jr. & Dalziel, I.W.D., 2003. Deep crustal structure of Bransfield Strait: initiation of a back arc basin by rift reactivation and propagation, *J. geophys. Res.*, **108**, 2492, doi:10.1029/2003JB002468.
- Dietrich, R., Rülke, A., Ihde, J., Lindner, K., Miller, H., Niemeier, W., Schenke, H.-W. & Seeber, G., 2004. Plate kinematics and deformation status of the Antarctic Peninsula based on GPS, *Glob. planet. Change*, **42**, 313–321.
- Dugda, M.T., Nyblade, A.A. & Julia, J., 2007. Thin lithosphere beneath the Ethiopian Plateau revealed by a joint inversion of Rayleigh wave group velocities and receiver functions, *J. geophys. Res.*, **112**, doi:10.1029/2006JB004918.
- Eagles, G., Gohl, K. & Larter, R.D., 2004. Life of the Bellingshausen plate, *Geophys. Res. Lett.*, **31**, L07603, doi:10.1029/2003GL019127.
- Eagles, G., Gohl, K. & Larter, R.D., 2009. Animated tectonic reconstruction of the Southern Pacific and alkaline volcanism at its convergent margins since Eocene times, *Tectonophysics*, **464**, 21–29.
- Forsyth, D.W., 1975. Fault plane solutions and tectonics of the South Atlantic and Scotia Sea, *J. geophys. Res.*, **80**, 1429–1443.
- Gambôa, L.A.P. & Maldonado, P.R., 1990. Geophysical investigation in the Bransfield Strait and in the Bellingshausen Sea – Antarctica, in *Antarctica as an Exploration Frontier—Hydrocarbon Potential, Geology and Hazards*, pp. 127–141, ed. St John, B., American Association of Petroleum Geologists.
- Gonzalez-Ferran, 1991. The Bransfield rift and its active volcanism, in *Geological Evolution of Antarctica*, pp. 505–509, eds Thomson, M.R.A., Crame, J.A. & Thomson, J.W., Cambridge University Press, Cambridge.
- Gràcia, E., Canals, M., Lí Farràn, M., José Prieto, M., Sorribas, J. & Team, G., 1996. Morphostructure and evolution of the central and Eastern Bransfield Basins (NW Antarctic Peninsula), *Mar. geophys. Res.*, **18**, 429–448.
- Gràcia, E., Canals, M., Farràn, M.L., Sorribas, J. & Pallas, R., 1997. Central and eastern Bransfield basins (Antarctica) from high-resolution swath-bathymetry data, *Antarct. Sci.*, **9**, 168–180.
- Grad, M., Guterch, A. & Janik, T., 1993. Seismic structure of the lithosphere across the zone of subducted Drake plate under the Antarctic plate, West Antarctica, *Geophys. J. Int.*, **115**, 586–600.
- Grad, M., Shiobara, H., Janik, T., Guterch, A. & Shimamura, H., 1997. Crustal model of the Bransfield Rift, West Antarctica, from detailed OBS refraction experiments, *Geophys. J. Int.*, **130**, 506–518.
- Green, W.V., Achauer, U. & Meyer, R.P., 1991. A 3-dimensional seismic image of the crust and upper mantle beneath the Kenya Rift, *Nature*, **354**, 199–203.
- Guterch, A., Grad, M., Janik, T., Perchuc, E. & Pajchel, J., 1985. Seismic studies of the crustal structure in West Antarctica 1979–1980—Preliminary results, *Tectonophysics*, **114**, 411–429.
- Guterch, A., Grad, M., Janik, T. & Perchuc, E., 1991. Tectonophysical models of the crust between the Antarctic Peninsula and the South Shetland Trench, in *Geological Evolution of Antarctica*, pp. 499–504, eds Thomson, M., Crame, J. & Thomson, J., Cambridge University Press, Cambridge.
- Heuret, A. & Lallemand, S., 2005. Plate motions, slab dynamics and back-arc deformation, *Phys. Earth planet. Inter.*, **149**, 31–51.
- Ibáñez, J.M., Morales, J., Alguacil, G., Almendros, J., Ortiz, R. & Del Pezzo, E., 1997. Intermediate-focus earthquakes under South Shetland Islands (Antarctica), *Geophys. Res. Lett.*, **24**, 531–534.
- Janik, T., 1997. Seismic crustal structure of the Bransfield Strait, West Antarctica, *Polish Polar Res.*, **18**, 171–225.
- Janik, T., Środa, P., Grad, M. & Guterch, A., 2006. Moho depths along the Antarctic Peninsula and crustal structure across the landward

- projection of the Hero fracture zone, in *Antarctica: Contributions to Global Earth Sciences*, pp. 229–236, eds Fütterer, D., Damaske, D., Kleinschmidt, G., Miller, H. & Tessensohn, F., Springer-Verlag, Berlin.
- Jarrard, R.D., 1986. Relations among subduction parameters, *Rev. Geophys.*, **24**, 217–284.
- Jin, Y.K., Larter, R.D., Kim, Y., Nam, S.H. & Kim, K.J., 2002. Post-subduction margin structures along Boyd Strait, Antarctic Peninsula, *Tectonophysics*, **346**, 187–200.
- Johnson, A.C., 1999. Interpretation of new aeromagnetic anomaly data from the central Antarctic Peninsula, *J. geophys. Res.*, **104**, 5031–5046.
- Karato, S., 1993. Importance of anelasticity in the interpretation of seismic tomography, *Geophys. Res. Lett.*, **20**, 1623–1626.
- Keller, G.R., Mechie, J., Braile, L.W., Mooney, W.D. & Prodehl, C., 1994. Seismic structure of the uppermost mantle beneath the Kenya rift, *Tectonophysics*, **236**, 201–216.
- Kennett, B.N.L. & Engdahl, E.R., 1991. Travel times for global earthquake location and phase identification, *Geophys. J. Int.*, **105**, 429–465.
- Kim, Y., Kim, H.-S., Larter, R.D., Camerlenghi, A., Gambôa, L.A.P. & Rudowski, S., 1995. *Tectonic Deformation in the Upper Crust and Sediments at the South Shetland Trench*, Antarctic Research Series Vol. 68, eds Cooper *et al.*, American Geophysical Union, Washington, DC.
- Larter, R.D. & Barker, P.F., 1991a. Effects of ridge crest-trench interaction on Antarctic-Phoenix spreading: forces on a young subducting plate, *J. geophys. Res.*, **96**, 19 583–19 607.
- Larter, R.D. & Barker, P.F., 1991b. Neogene interaction of tectonic and glacial processes at the Pacific margin of the Antarctic Peninsula, in *Sedimentation, Tectonics and Eustasy*, pp. 165–186, ed. Macdonald, D.I.M., Blackwell, Oxford.
- Larter, R.D., Cunningham, A.P., Barker, P.F., Gohl, K. & Nitsche, F.O., 2002. Tectonic evolution of the Pacific margin of Antarctica 1. Late Cretaceous tectonic reconstructions, *J. geophys. Res.*, **107**, 2345, doi:10.1029/2000JB000052.
- Larter, R.D., Vanneste, L.E., Morris, P. & Smythe, D.K., 2003. Structure and tectonic evolution of the South Sandwich arc, *Geol. Soc. London, Spec. Publ.*, **219**, 255–284, doi:10.1144/GSL.SP.2003.219.01.13.
- Lawver, L.A., Keller, R.A., Fisk, M.R. & Strelin, J.A., 1995. Bransfield Strait, Antarctic Peninsula: active extension behind a dead arc, in *Back-Arc Basins: Tectonics and Magmatism*, pp. 315–342, ed. Taylor, B., Plenum Press, New York, NY.
- Lawver, L.A., Sloan, B.J., Barker, D.H.N., Ghidella, M., Herzen, R.P.V., Keller, R.A., Klinkhammer, G.P. & Chin, C.S., 1996. Distributed active extension in Bransfield Basin, Antarctic Peninsula: evidence from multi-beam bathymetry, *GSA Today*, **6**, 1–6.
- Lee, D.K., Jin, Y.K., Kim, Y. & Nam, S.H., 2000. Seismicity and tectonics around the northern Antarctic Peninsula from King Sejong station data, *Antarct. Sci.*, **12**, 196–204.
- Livermore, R. *et al.*, 2000. Autopsy on a dead spreading center: the Phoenix Ridge, Drake Passage, Antarctica, *Geology*, **28**, 607–610.
- Livermore, R.A., 2003. Back-arc spreading and mantle flow in the East Scotia Sea, *Geol. Soc. London, Spec. Publ.*, **219**, 315–331, doi:10.1144/GSL.SP.2003.219.01.15.
- Maldonado, A., Larter, R.D. & Aldaya, F., 1994. Forearc tectonic evolution of the South Shetland Margin, Antarctic Peninsula, *Tectonics*, **13**, 1345–1370.
- Mechie, J., Fuchs, K. & Altherr, R., 1994. The relationship between seismic velocity, mineral composition and temperature and pressure in the upper mantle—with an application to the Kenya Rift and its eastern flank, *Tectonophysics*, **236**, 453–464.
- Nyblade, A.A., Knox, R.P. & Gurrrola, H., 2000. Mantle transition zone thickness beneath Afar: implications for the origin of the Afar hotspot, *Geophys. J. Int.*, **142**, 615–619.
- Park, Y. & Nyblade, A.A., 2006. P-wave tomography reveals a westward dipping low velocity zone beneath the Kenya Rift, *Geophys. Res. Lett.*, **33**, L07311–L07314.
- Park, Y., Nyblade, A.A., Rodgers, A.J. & Al-Amri, A., 2007. Upper mantle structure beneath the Arabian Peninsula and Northern Red Sea from teleseismic body wave tomography: implications for the origin of Cenozoic uplift and volcanism in the Arabian Shield, *Geochem. Geophys. Geosyst.*, **8**, doi:10.1029/2006GC001566.
- Pelayo, A.M. & Wiens, D.A., 1989. Seismotectonics and relative plate motions in the Scotia Sea Region, *J. geophys. Res.*, **94**, 7293–7320.
- Ritsema, J., Nyblade, A.A., Owens, T.J., Langston, C.A. & VanDecar, J.C., 1998. Upper mantle seismic velocity structure beneath Tanzania, east Africa: implications for the stability of cratonic lithosphere, *J. geophys. Res.-Solid Earth*, **103**, 21 201–21 213.
- Robertson Maurice, S.D., Wiens, D.A., Shore, P.J., Vera, E. & Dorman, L.M., 2003. Seismicity and tectonics of the South Shetland Islands and Bransfield Strait from a regional broadband seismograph deployment, *J. geophys. Res.*, **108**, 2461, doi:10.1029/2003JB002416.
- Sandwell, D.T., 1992. Antarctic marine gravity field from high-density satellite altimetry, *Geophys. J. Int.*, **109**, 437–448.
- Sato, H., Sacks, I.S., Murase, T. & Scarfe, C.M., 1988. Thermal structure of the low velocity zone derived from laboratory and seismic investigations, *Geophys. Res. Lett.*, **15**, 1227–1230.
- Scheuer, C., Gohl, K., Larter, R.D., Rebesco, M. & Udintsev, G., 2006. Variability in Cenozoic sedimentation along the continental rise of the Bellingshausen Sea, West Antarctica, *Mar. Geol.*, **227**, 279–298.
- Smellie, J.L., Pankhurst, R.J., Thomson, M.A. & Davies, R.E.S., 1984. The geology of the south Shetland Islands: VI. Stratigraphy, geochemistry and evolution, British Antarctic Survey Scientific Report, 85pp.
- Stern, R.J., 2002. Subduction zones, *Rev. Geophys.*, **40**, 1012, doi:10.1029/2001RG000108.
- Tucholke, B.E. & Houtz, R.E., 1976. Sedimentary framework of the Bellingshausen Basin from seismic profiler data, *Initial Rep. Deep Sea Drill. Proj.*, **35**, 197–227.
- VanDecar, J.C., 1991. Upper mantle structure of the Cascadia subduction zone from non-linear teleseismic travel time inversion, *PhD thesis*, Univ. of Washington, Seattle, WA.
- VanDecar, J.C. & Crosson, R.S., 1990. Determination of teleseismic relative phase arrival times using multi-channel cross-correlation and least-squares, *Bull. seism. Soc. Am.*, **80**, 150–169.
- Venkataraman, A., Nyblade, A.A. & Ritsema, J., 2004. Upper mantle Q and thermal structure beneath Tanzania, East Africa from teleseismic P wave spectra, *Geophys. Res. Lett.*, **31**, doi:10.1029/2004GL020351.
- Vuan, A., Cazzaro, R., Costa, G., Russi, M. & Panza, G.F., 1999. S-wave velocity models in the Scotia Sea region, Antarctica, from nonlinear inversion of Rayleigh waves dispersion, *Pure appl. Geophys.*, **154**, 121–139.
- Vuan, A., Russi, M. & Panza, G.F., 2000. Group velocity tomography in the subantarctic Scotia Sea region, *Pure appl. Geophys.*, **157**, 1337–1357.
- Vuan, A., Brancolini, G., Panza, G.F., Russi, M. & Wu, F., 2001. Joint inversion of receiver function of teleseismic body waves and local group velocity dispersion curves beneath ESPZ and PMSA stations (Antarctic Peninsula), *Terra Antarctica*, **8**, 49–54.
- Vuan, A., Lodolo, E., Panza, G.F. & Sauli, C., 2005a. Crustal structure beneath Discovery Bank in the Scotia Sea from group velocity tomography and seismic reflection data, *Antarct. Sci.*, **17**, 97–106.
- Vuan, A., Robertson Maurice, S.D., Wiens, D.A. & Panza, G.F., 2005b. Crustal and upper mantle S-wave velocity structure beneath the Bransfield Strait (West Antarctica) from regional surface wave tomography, *Tectonophysics*, **397**, 241–259.
- Yegorova, T., Bakmutov, V., Janik, T. & Grad, M., 2011. Joint geophysical and petrological models for the lithosphere structure of the Antarctic Peninsula continental margin, *Geophys. J. Int.*, **184**, 90–110.

SUPPORTING INFORMATION

Additional Supporting Information may be found in the online version of this article:

Figure S1. Synthetic checkerboard resolution test.

Please note: Wiley-Blackwell are not responsible for the content or functionality of any supporting materials supplied by the authors. Any queries (other than missing material) should be directed to the corresponding author for the article.